Catalysis Science & Technology

ROYAL SOCIETY OF CHEMISTRY

PAPER

View Article Online
View Journal | View Issue

Cite this: *Catal. Sci. Technol.*, 2023, 13, 4420

Iron-doped Co_3O_4 catalysts prepared by a surfactant-assisted method as effective catalysts for malic acid oxidative decarboxylation

Gheorghiţa Mitran, *[a] Ştefan Neaţu, [b] Octavian Dumitru Pavel, [a] Adriana Urdă,[a] Anca G. Mirea,[b] Mihaela Florea [ab] and Florentina Neaţu *[b]

Received 25th January 2023,
Accepted 18th June 2023

DOI: 10.1039/d3cy00121k

rsc.li/catalysis

Iron-doped Co_3O_4 oxides prepared by a surfactant-assisted method exhibited good catalytic activity in malic acid conversion, and the oxygen defects associated with the presence of Co^{2+} played a key role in catalyst activation for pyruvic acid production. The most active catalyst, for which the malic acid conversion was 70% and the pyruvic acid yield was 24%, has an inverse spinel type structure (Fe^{3+} replaces Co^{2+} from tetrahedral sites, while Fe^{2+} replaces Co^{3+} from octahedral sites) as well as a small energy difference between the highest occupied orbital and the lowest unoccupied orbital (low band-gap, E_g). The catalyst with the highest Co^{2+} loading showed the highest yield of pyruvic acid.

1. Introduction

Malic acid is among the first 12 chemicals produced from renewable sources of carbohydrates, and can later be transformed into a variety of high-value biochemicals, so its world market reaches 200 000 tons per year.[1]

The L-malic acid enantiomer, known as "apple acid", is the only one that exists in nature in fruits and vegetables, particularly in apples, while the D-malic acid enantiomer does not exist in nature. A mixture of DL-malic acid enantiomers is produced through industrial synthesis[2,3] as well as by the enzymatic hydration of fumarate, the latter method being under development. Considering the global trend at the industrial level to find viable solutions for oil-based compounds, malic acid production through enzymatic fermentation has gained more attention. In this regard, the industrial interest in the production of malic acid by microbial fermentation has increased, especially through the classic tricarboxylic acid (TCA) cycle, which converts 1 mole of glucose into 2 moles of malic acid. There are also many other methods for malic acid production, some of them focusing on the use of glycerol as a raw material, but active microorganisms for this process are still sought after.[4,5]

Malic acid is primarily used as a substrate in the production of homo- and heteropolymers, such as polymalic acid (by ring-opening polymerization or polycondensation), a biodegradable, bioabsorbable, water soluble and innovative bio-polymer[6] with medical applications by the introduction of drugs into its polymer chain. It also has applications in the pharmaceutical field as a component of the migraine drug almotriptan malate, in the semiconductor industry as a polishing and cleaning material, and also as an animal feed additive.[7]

Pyruvic and malonic acids can be obtained through photocatalytic oxidation of malic acid using a TiO_2-coated optical fiber reactor[8] or an illuminated aqueous suspension of TiO_2.[9] Pyruvic acid represents a precursor for pharmaceutical chemicals (such as tryptophan, tyrosine, cysteine, leucine, vitamin B12 and vitamin B6),[10] a functional additive for beverages[11] and a substrate for pesticide synthesis.[12] The traditional route for pyruvic acid synthesis is tartaric acid pyrolysis, a method with several environmental and economic disadvantages. Malonic acid is widely used in the production of pharmaceuticals, petrochemicals and cosmetics. The traditional route for malonic acid production consists of petrochemical processes using fossil resources.[13]

Biomass-derived acid decarboxylation is applied in the chemical industry as a method for obtaining valuable products, such as alkanes, alkenes with fuel and synthetic applications,[14] carbonyl compounds with applications as solvents and as feed for bulk chemicals,[15] ethers, and nitriles.[16,17]

Transition metal oxides belonging to the iron series, such as Co_3O_4, have been developed and used as catalysts,

[a] *Department of Inorganic, Organic Chemistry, Biochemistry & Catalysis, Faculty of Chemistry, University of Bucharest, 4-12, Blv. Regina Elisabeta, 030018 Bucharest, Romania. E-mail: geta.mitran@chimie.unibuc.ro, geta_mitran@yahoo.com*
[b] *National Institute of Material Physics, 405A Atomiştilor Street, PO Box MG 7, 077125 Măgurele, Romania. E-mail: florentina.neatu@infim.ro*

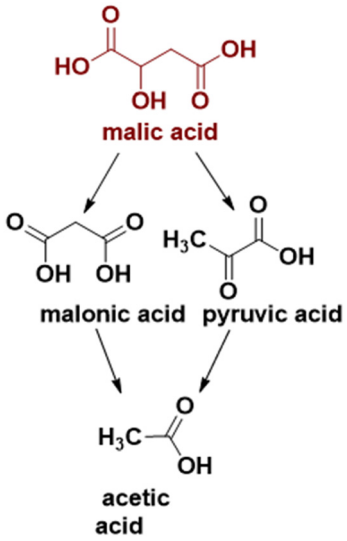

Scheme 1 Malic acid conversion to products.

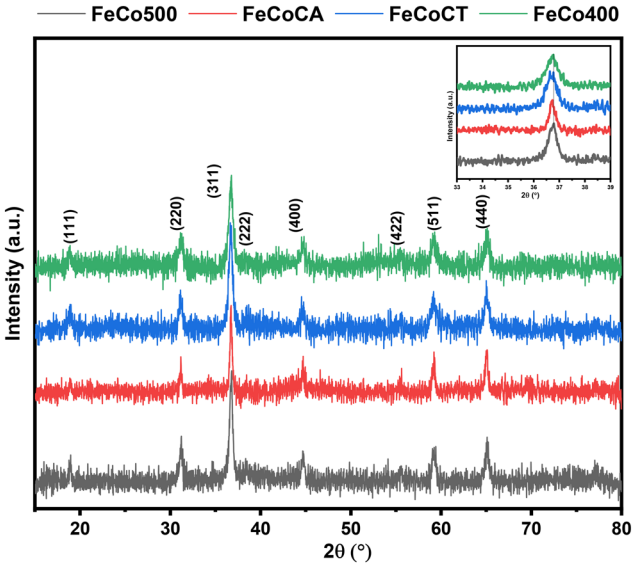

Fig. 1 XRD patterns of Fe–Co spinel oxides: FeCo400 (calcined 400), FeCo500 (calcined 500), FeCoCA (citric acid), and FeCoCT (CTAB).

particularly for the purpose of selective oxidation of alcohols,[18–20] and oxygen reduction.[21] These catalysts possess advantageous properties, such as redox properties, cost-effectiveness, eco-friendliness and uncomplicated synthesis methods.[22–24]

Many synthesis methods have been used to control the phase composition, homogeneity, purity and microstructure of Co_3O_4 materials;[25,26] however, many

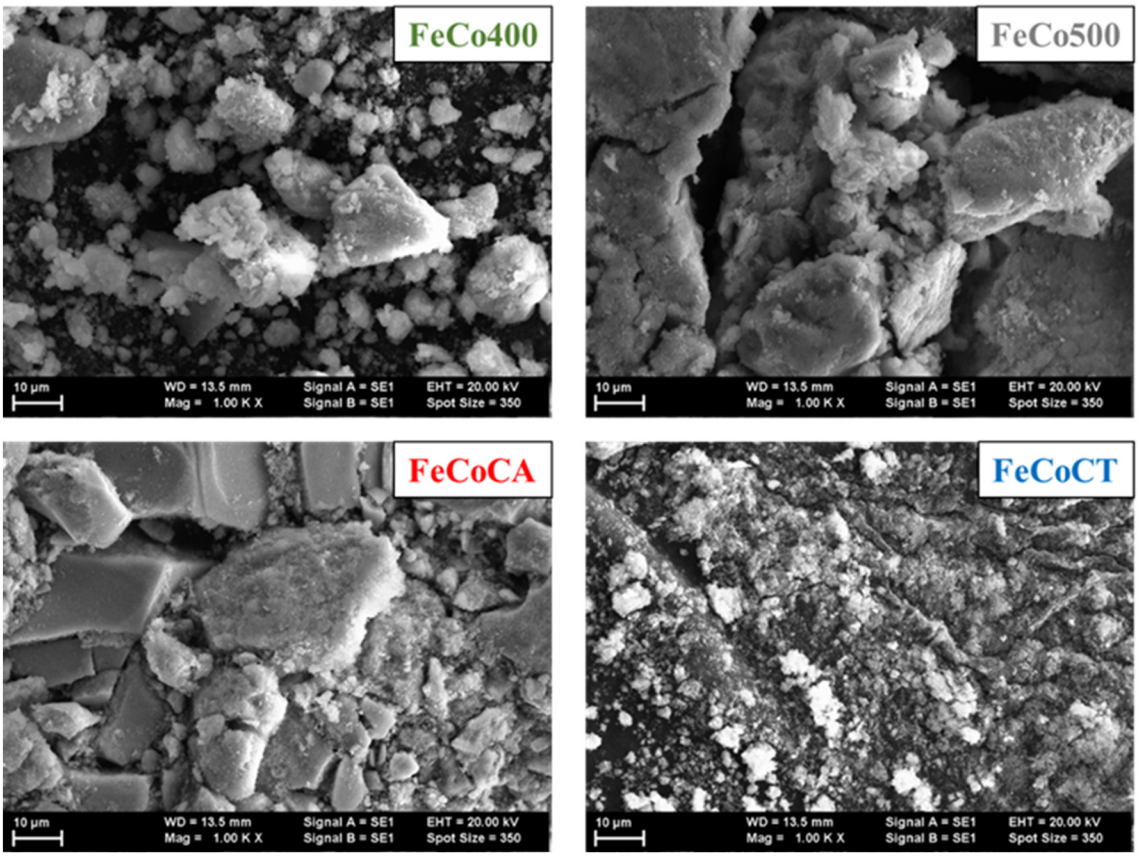

Fig. 2 SEM images of Fe–Co spinel oxides: FeCo400 (calcined 400), FeCo500 (calcined 500), FeCoCA (citric acid), and FeCoCT (CTAB).

challenges remain in terms of the synthesis method, the factors that influence the network structure and texture remaining to be determined. Organic surfactants were used in order to control the growth, taking into account the tendency of Co_3O_4 to form larger and irregular particles. Wang *et al.*[27] reported the synthesis of Co_3O_4 using a surfactant-assisted method in the presence of cetyltrimethylammonium bromide (CTAB) yielding nanomaterials with diameters ranging from 15 to 25 nm. Deng *et al.*[28] used a citrate gel combustion method to investigate the effect of changing the fuel ratio on the phase composition and morphology, an excess of fuel leading to a transformation from granular Co_3O_4 aggregates with a cubic structure to a mixture of cubic Co_3O_4 and tetragonal CoO phases. At the same time, Singhal *et al.*[29] reported a solution combustion method in the presence of urea, obtaining particles around 50–70 nm in size, with a hexagonal morphology.

To the best of our knowledge, no study regarding the influence of iron doping on the catalytic properties of cobalt spinel oxides in malic acid oxidative dehydrogenation/decarboxylation exists in the literature so far. In the present study, we report the synthesis of iron-doped Co_3O_4 nanoparticles using a surfactant-assisted method, as well as the correlation of their physicochemical properties with the catalytic activity in the conversion of malic acid to pyruvic, acetic and malonic acids (see Scheme 1).

2. Experimental section

2.1. Catalyst preparation

Samples with the formula $Fe_{0.15}Co_{2.85}O_4$ were synthesized by co-precipitation of cobalt and iron precursors with ammonium carbonate with and without surfactants, such as citric acid and cetyltrimethylammonium bromide (CTAB). In the first stage, two solutions were prepared, a mixed solution consisting of $Fe(NO_3)_3{\cdot}9H_2O$ (AGR ACS Labbox) and $Co(NO_3)_2{\cdot}6H_2O$ (AGR ACS Labbox), and a solution of surfactant, such that the molar ratio of surfactant/(Co + Fe) was 0.04. These two solutions were first separately prepared and magnetically stirred for 30 minutes (the CTAB solution was heated to 60 °C and then cooled) by using a stirring speed of 600 rpm and later were mixed together. In the second stage, to the above-mentioned mixture, a solution (0.5 M) of ammonium carbonate, $(NH_4)_2CO_3$ (ROTH), was added dropwise, the final molar ratio of (Co + Fe)/NH_4 being 1 : 2. The precipitation took place at ambient temperature and at a pH value between 8 and 9.

The product was later filtered, washed several times with distilled water, and then dried at 100 °C for 24 h. The resulting solid was calcined at 500 °C for 4 h, except for the two samples prepared in the absence of surfactants that were calcined both at 400 °C and 500 °C, respectively. The final solids were named as follows: FeCo400 (calcined 400), FeCo500 (calcined 500), FeCoCA (citric acid), and FeCoCT (CTAB).

Table 1 Composition data of Fe–Co spinel oxides calculated from the EDX results

Element/sample	Co	Fe	O
FeCo400	78.55	4.21	17.23
FeCo500	75.78	3.9	20.31
FeCoCA	83.65	4.27	12.06
FeCoCT	66.67	3.54	29.77

2.2. Catalyst characterization

X-ray diffraction (XRD) analysis of the powders was carried out with a Bruker-AXS D8 Advance diffractometer (Bruker

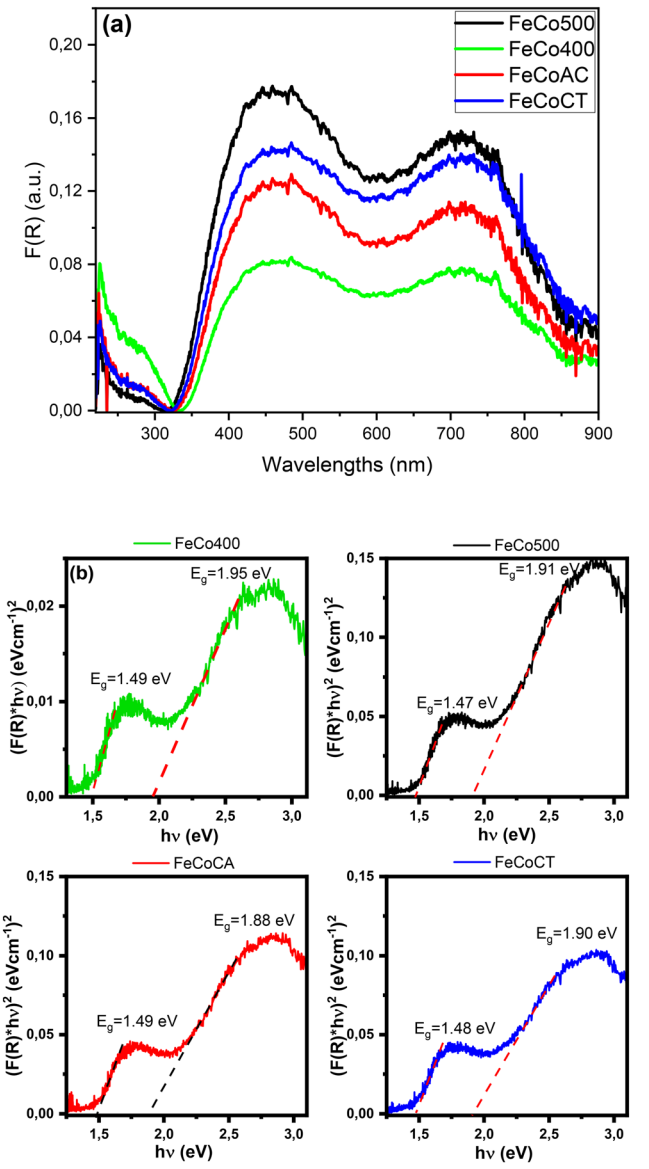

Fig. 3 UV-vis absorption spectra of Fe–Co spinel oxides (a), and the absorption band gap E_g of the samples (b).

Corporation, Billerica, MA, USA) equipped with a LynxEye 1D type detector and a Cu-K_α (0.1541 nm) radiation source, in the 2θ range of 10–80°.

The morphology of the samples was investigated by scanning electron microscopy (SEM) and the composition by energy dispersive X-ray spectroscopy (EDX) using a Zeiss EVO 50 XVP scanning electron microscope equipped with a Quantax Bruker 200 system as an attachment.

Diffuse reflectance UV-vis spectra were recorded on $BaSO_4$ diluted powders using a Jasco V-650 spectrometer fitted with a D2/WI light source, with a JSV-9222 integrating sphere and built-in PMT detector, with a scan speed of 1000 nm min^{-1}, a data interval of 0.5 nm and a measurement range of 900–200 nm.

The FTIR spectra of all prepared samples were acquired both in ATR and DRIFT mode by using a Jasco FT/IR 4700 type A infrared spectrometer, with a standard light source, a TGS detector, a resolution of 4 cm^{-1} and a scanning speed of 2 mm s^{-1}.

A Kratos Ultra DLD Setup (Kratos Analytical Ltd., Manchester, UK) was used to record the XPS data. Al K radiation (1486.74 eV) was used as the radiation source, with a monochromated X-ray source with a total power of 300 W; for analyses a pressure of 1×10^{-7} Pa was used in the analysis chamber. For the binding-energy values, a signal-calibrating standard was used with C 1s at 284.8 eV.

All samples' Raman spectra were recorded at room temperature in the range of 100–800 cm^{-1} on a Horiba Jobin Yvon LabRAM HR Evolution spectrometer outfitted with a cooled Sincerity CCD Peltier-cooled detector and a 633 nm air-cooled He–Ne laser. The spectra were obtained by averaging 5 accumulations of 50 s of laser exposure. By adjusting the laser power (9.7 mW) with a 25% neutral density filter, the degradation of the samples was avoided.

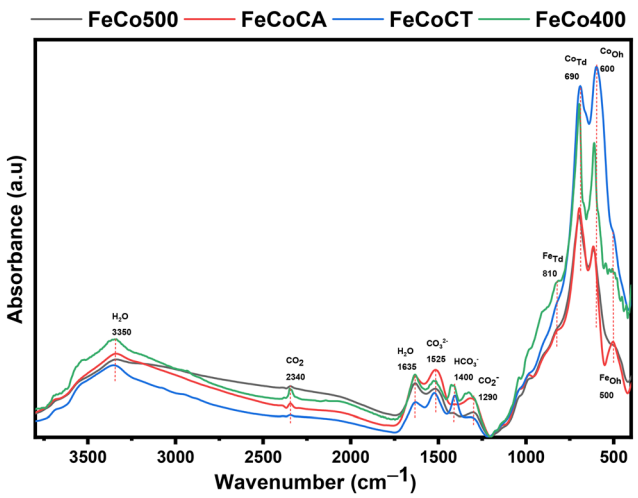

Fig. 4 DRIFT spectra of Fe–Co spinel oxides: FeCo400 (calcined 400), FeCo500 (calcined 500), FeCoCA (citric acid), and FeCoCT (CTAB).

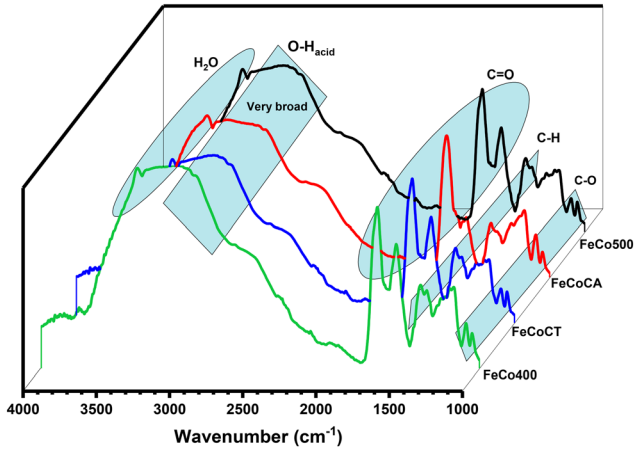

Fig. 5 FTIR-ATR spectra of all samples after malic acid conversion toward pyruvic and acetic acid.

2.3. Catalytic tests

The catalytic tests were performed in the oxidative dehydrogenation/decarboxylation reactions of L-malic acid. The oxidative dehydrogenation/decarboxylation reactions were carried out in the liquid phase by using a two-necked flat bottomed boiling flask (25 mL) placed on a heated magnetic stirrer. Different solutions of malic acid in water or ethanol (with concentrations of 2, 3.5 and 5 wt%) were added in the flask and stirred, with a stirring speed of 400 rpm, in the presence of air as an oxidant (20 mL min^{-1}), up to a temperature of 50 °C. Then, the catalyst (0.05 g) was added to start the reaction. Aliquots from the solution were taken out at regular time intervals and analyzed with the help of a gas-chromatograph (Thermo-Quest GC K072320) equipped with a flame ionization detector (FID).

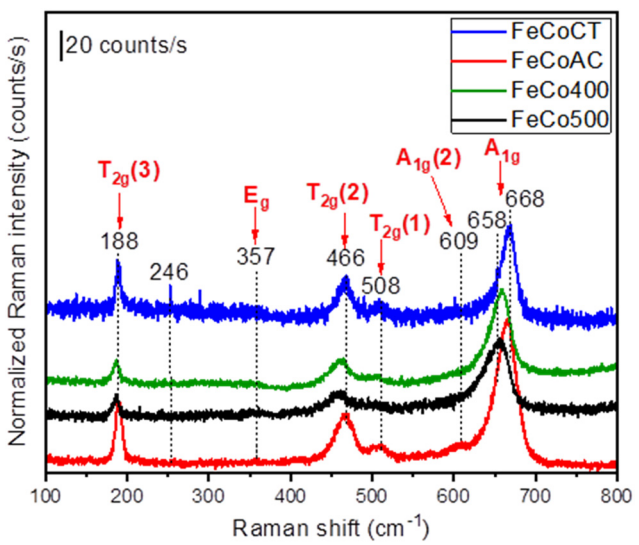

Fig. 6 Raman spectra of Fe–Co oxides: FeCo400 (calcined 400), FeCo500 (calcined 500), FeCoCA (citric acid), and FeCoCT (CTAB).

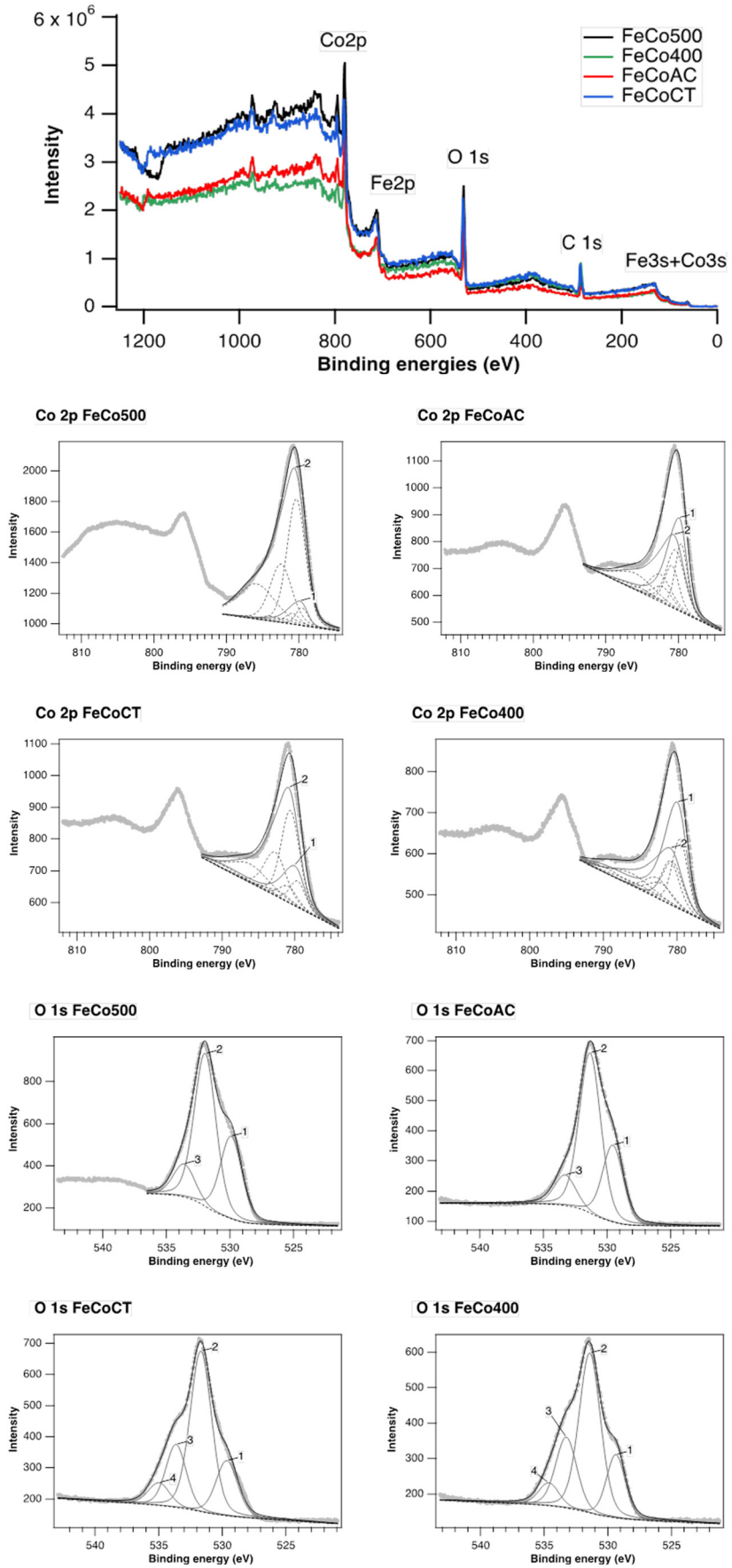

Fig. 7 XPS spectra of the Fe–Co oxides.

Table 2 The composition of Co_3O_4 and CoO from the XPS spectra

	FeCo500	FeCoCA	FeCoCT	FeCo400
Co_3O_4 – multiplet 1	9	45	23	58
CoO – multiplet 2	91	55	77	42

3. Results and discussion

3.1. Catalyst characterization

The XRD patterns are shown in Fig. 1 and can be linked to the presence of the AB_2O_4 cubic phase with a spinel structure, where A and B correspond to tetrahedral and octahedral cations sites, respectively. As shown, the main diffraction line of the (311) plane is situated at 2θ = 36.8°. The presence of a shoulder at lower values of 2θ degrees and even a splitting of this line in the case of the FeCoCT sample, can be correlated with the coexistence of both normal and inverse spinel phases.[30,31] In the regular spinel, Fe^{3+} replaces the Co^{3+} ions from the octahedral sites; however, in the inverse spinel, Co^{2+} from the tetrahedral sites is replaced with Fe^{3+}, while Co^{3+} cations from the octahedral sites are replaced by Fe^{2+} cations. When compared to other samples, the main diffraction line of the (311) plane for the sample FeCoCA is shifted towards the lower angle side; this could be due to defects induced in the crystalline structure in the presence of citric acid as a surfactant.

The morphology of the samples was investigated by the SEM method (Fig. 2) and a granular structure can be observed for all samples. The different nanograins on the surface did not have large size variations and a porous structure between different grains was also evidenced.

The elemental composition of the samples was evaluated by analyzing different sample regions by the EDX technique. The composition data calculated from the EDX results are summarized in Table 1.

The ratio between Fe and Co obtained by EDX is almost the same as the theoretical one for all samples, indicating that the co-precipitation was efficient with or without the surfactant.

The optical absorption spectra shown in Fig. 3a present two broad bands in the 400–500 nm and the 650–800 nm regions that are given by the $O^{2-} \rightarrow Co^{2+}$ and the $O^{2-} \rightarrow Co^{3+}$ charge-transfer transitions, respectively.[32] The broad band in the region 650–800 nm showed three maxima located at 715 nm (Co^{3+}), as well as at 745 and 770 nm corresponding to iron ions,[33–35] visible especially on the FeCoCT catalyst.

In order to identify the centers responsible for the catalytic activity in mixed metal oxides, it is useful to know the chemical properties of both the metal centers and the oxygen. A factor that describes both the nature of the active oxygen centers and the tendency of the adjacent metal centers to gain electron density is represented by the ligand to metal charge transfer excitation energy (LMCT), which corresponds to the band-gap energy.[36]

The absorption band-gap E_g of the samples was determined using the following equation:

$$(F(R)hv)^n = a(hv - E_g)$$

where h is Planck's constant, v is the frequency of light, $F(R)$ is the Kubelka–Munk function, a represents a constant independent of the energy, and E_g is the optical band gap, while n is 2 for an indirect transition or 1/2 to a direct transition.[37] The indirect bandgaps, better correlated with the experimental data, were determined by plotting $(F(R)hv)^2$ as a function of hv (Fig. 3b).

The energy gap values were given by the interception of the two straight line portions. The values are situated in the range of ~1.47–1.49 eV for the lower energy side region and ~1.88–1.95 eV for the higher energy side region, in good agreement with the literature data.[38–40] The relatively high values highlight the presence of a small crystallite size and partial amorphous structure.

DRIFT studies (Fig. 4) were performed in order to confirm the nature of functional groups present on our samples. The band at 1290 cm^{-1} is assigned to carboxylate (COO^-), and that at 1400 cm^{-1} to bicarbonate species (HCO_3^-), while the band located at 1525 cm^{-1} is assigned to carbonate species (CO_3^{2-}) on the catalyst surface.[41,42]

The band of tetrahedral sites is located at a higher wavenumber than that of octahedral sites, due to the fact that tetrahedral positions have smaller bond lengths compared with the octahedral positions.[43] The bands at 690 cm^{-1} and 600 cm^{-1} are assigned to vibrational modes of cobalt–oxygen, Co–O, in Co_3O_4.[44] The absorption band at 500 cm^{-1} is linked with stretching modes of the Fe^{3+} octahedral sites and that at 810 cm^{-1} is associated with iron ion vibration in tetrahedral coordination.[45]

Fig. 5 depicts the FTIR-ATR spectra of the catalysts after malic acid conversion. The broad band in the 3000–3300 cm^{-1} range is associated with –OH groups of carboxyls and that at 3400 cm^{-1} with H_2O molecule absorption.[46] The carbonyl C═O species present bands at 1720–1750 cm^{-1}, and the band at 1440 cm^{-1} is assigned to –CH bonds, while the bands at 1060 and 1100 cm^{-1} are assigned to C–O stretches.

Raman spectroscopy was employed to check the presence of any non-crystalline secondary phases that might not be identified by XRD. The Raman spectra of the FeCo samples synthesized in this study are shown in Fig. 6. As revealed by the XRD analysis, the FeCo samples are not fully normal spinel type, with a mixture of both normal and inverse spinel types co-existing. As part of the space group *Fd3m*, the Co_3O_4 oxides crystallize in cubic structures, with such structures presenting five Raman active phonon modes, namely A_{1g}, E_g and $^3T_{2g}$. However, any cation redistribution in the tetrahedral and octahedral sites of the Co_3O_4 normal spinel will alter the symmetry of the crystal structure into the $I4_1/amd$ space group that can show up to ten active vibrational modes in the Raman spectrum.

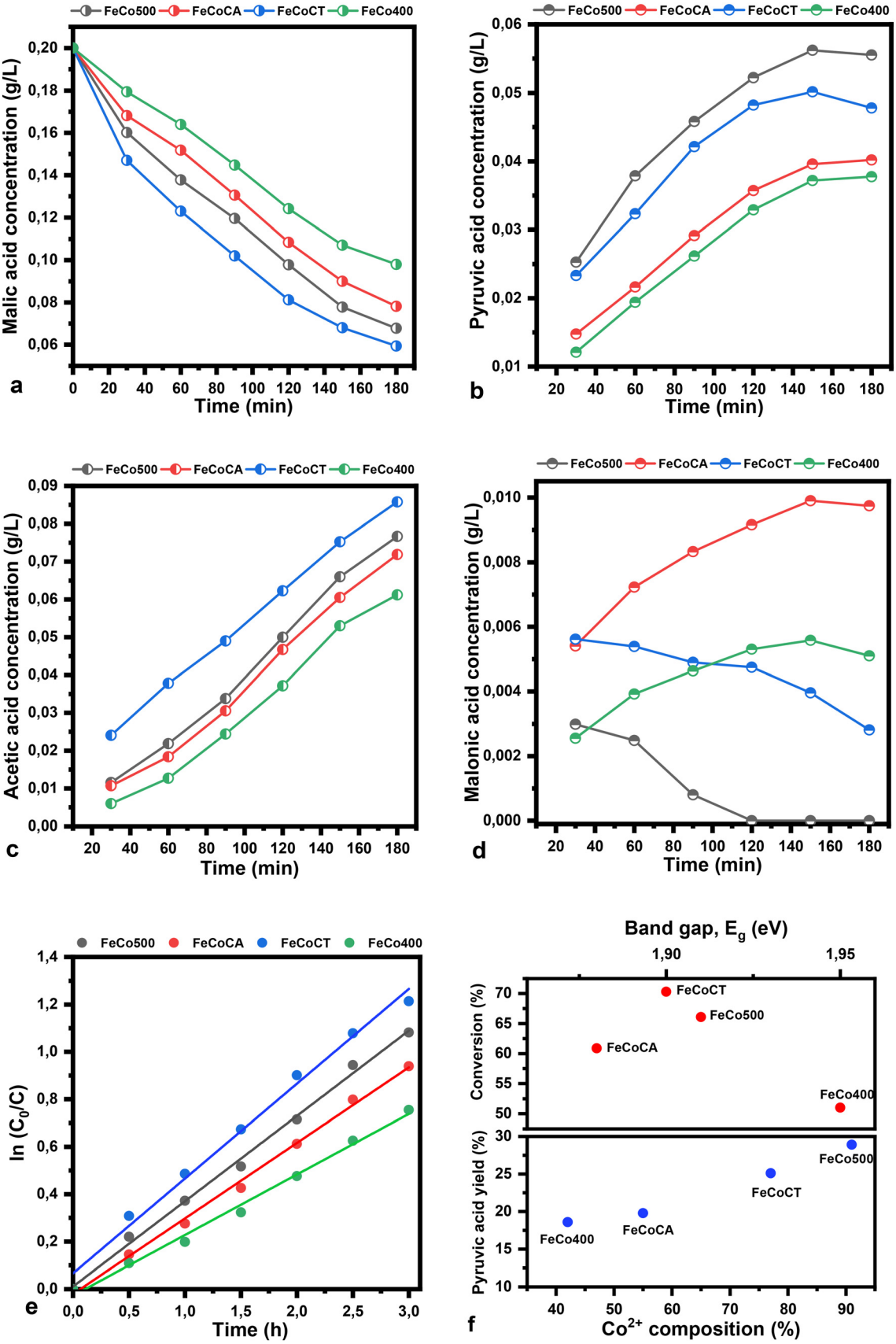

Fig. 8 The plot of the malic acid concentration (a), and pyruvic (b), acetic (c) and malonic acid concentration (d) *versus* time (the reaction conditions – solvent: ethanol, temperature: 50 °C, catalyst loading: 1%, air flow: 20 mL min^{-1}, stirring speed: 400 rpm); $\ln(C_0/C)$ *versus* time plot (e), malic acid conversion *versus* band gap and pyruvic acid yield *versus* Co^{2+} composition (f).

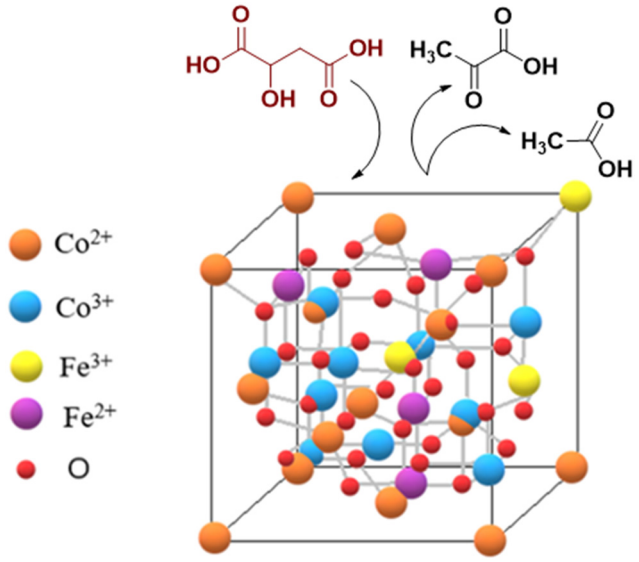

Scheme 2 Malic acid conversion on the inverse spinel structure.

In our case, all samples show more than five peak maxima at 188, 357, 466, 508, 609 and 655 or 668 cm^{-1}. In accordance with the literature, the frequencies above 600 cm^{-1} are due to A_{1g} symmetry involving symmetric stretching of an oxygen atom with respect to the metal ion in the tetrahedral void, the so-called tetrahedral breath mode since only oxygen atoms are moving.[47] The peak maxima located at 668 cm^{-1} (for the case of the FeCoCT and FeCoCA samples) and 658 cm^{-1} (for the case of the FeCo400 and FeCo500 samples) are characteristic for the cubic spinel-type structure, while the presence of an additional mode designated as the $A_{1g(2)}$ mode (located at 609 cm^{-1}) is a characteristic of inverse as well as mixed spinel compounds. The average shift of ~10 cm^{-1} between the peak maxima related to the A_{1g} mode may be attributed to size effects or surface stress/strain.

At lower frequencies below 600 cm^{-1}, the observed phonon modes (E_g and $^3T_{2g}$ modes located at 357 and 508, 466 and 188 cm^{-1}, respectively) are attributed to the symmetric and antisymmetric bending of oxygen atoms in M–O bonds at octahedral voids.[48,49]

Besides these phonon modes, in the case of the FeCo500 sample, the presence of a secondary peak located at 246 cm^{-1} and attributed to the E_g mode of α-Fe_2O_3 (ref. 50) indicates the formation of a common impurity that typically is formed during the synthesis of spinel-type catalysts.[51]

XPS spectra of all prepared samples are shown in Fig. 7. The general spectra show the presence of C, O, Co and Fe. The high-resolution spectra of Fe 2p and Fe 3s give us information about the existence of Fe, but unfortunately, no quantitative information about the oxidation states of Fe can be extracted, due to the auger lines of Co overlapping with the Fe 2p signal. Moreover, the Co 3s lines overlap with the Fe 3s signal. From the high-resolution spectrum of Co 2p, the presence of two fingerprints specific to different oxidation states of Co can be observed: the multiplet 1 Co_3O_4 footprint containing both Co(II) and Co(III) and the multiplet 2 footprint specific to CoO, with Co(II) surrounding the specific CoO structure. Different percentages of the two cobalt components are observed depending on the preparation method (see Table 2). Thus, FeCo500 and FeCoCT materials contain a small amount of up to ~20% Co_3O_4 phase, while FeCo400 and FeCoCA materials show a mixture of the two components Co_3O_4 and CoO, respectively. The peak area of Co^{2+} is higher than that of Co^{3+} in FeCo500 and FeCoCT, which indicates the oxygen vacancy generation accompanying Co^{2+}.[52]

Deconvolution of the O 1s spectra reveals the presence of three types of oxygen on the surface: the oxygen of carbonate species (peak 2) centered at 531.8 eV, along with two other peaks centered at 529.6 eV corresponding to lattice oxygen (peak 1) and at 533.5 eV, corresponding to hydroxyl groups (peak 3), the FeCoCT and FeCo400 having a higher amount of OH on the surface compared to the other two samples. In addition, in these two samples, a fourth peak appears at 534.8 eV, specific to water chemisorbed on the surface (peak 4).

3.2. Catalytic experiments

Effect of solvent. In this study, malic acid oxidative dehydrogenation/decarboxylation to pyruvic, acetic and malonic acid, respectively, has been carried out on iron-doped Co_3O_4 catalysts prepared in the presence or absence of surfactants. Fig. 8 depicts the concentration profile for malic acid (in ethanol as a solvent) and the reaction products as a function of time. The concentration of malic acid appears to have been halved after 1.5 hours of reaction, whereas the concentration of pyruvic acid appears to have reached a maximum after 2.5 hours of reaction. The conversion of malic acid (Fig. 8a) evolved as a function of the catalyst as follows: FeCoCT > FeCo500 > FeCoCA > FeCo400, in the same way as the energy band gap decreased, except for the FeCoCA sample, which is probably due to the presence of a large amount of octahedral iron on the surface (as can be seen in the DRIFT spectrum) and the presence of an inverse spinel structure (Scheme 2), while the pyruvic acid yield increased with increasing oxygen defects, associated with the presence of Co^{2+} (Fig. 8f). The concentration of pyruvic acid reaches maximum values (Fig. 8b) for the catalysts with a larger number of tetrahedral sites, as observed from the DRIFT spectra. Acetic acid (Fig. 8c) has almost the same tendency as pyruvic acid, but is obtained in a larger amount. The electronic transfer that occurred in the redox reactions can be correlated with the existence of a low value of band gap energy, which allows greater mobility of electrons in the catalytic reaction, in accordance with the results obtained by Kouotou *et al.*[53] in the oxidation of CO over Fe_3O_4 catalysts, who noticed an improvement in the catalytic activity when the E_g value decreased. Similar results were also reported by Getsoian *et al.*[36] in propene oxidation over mixed metal oxides as well as by Kasmi *et al.*[54] and Jibril *et al.*[55] in

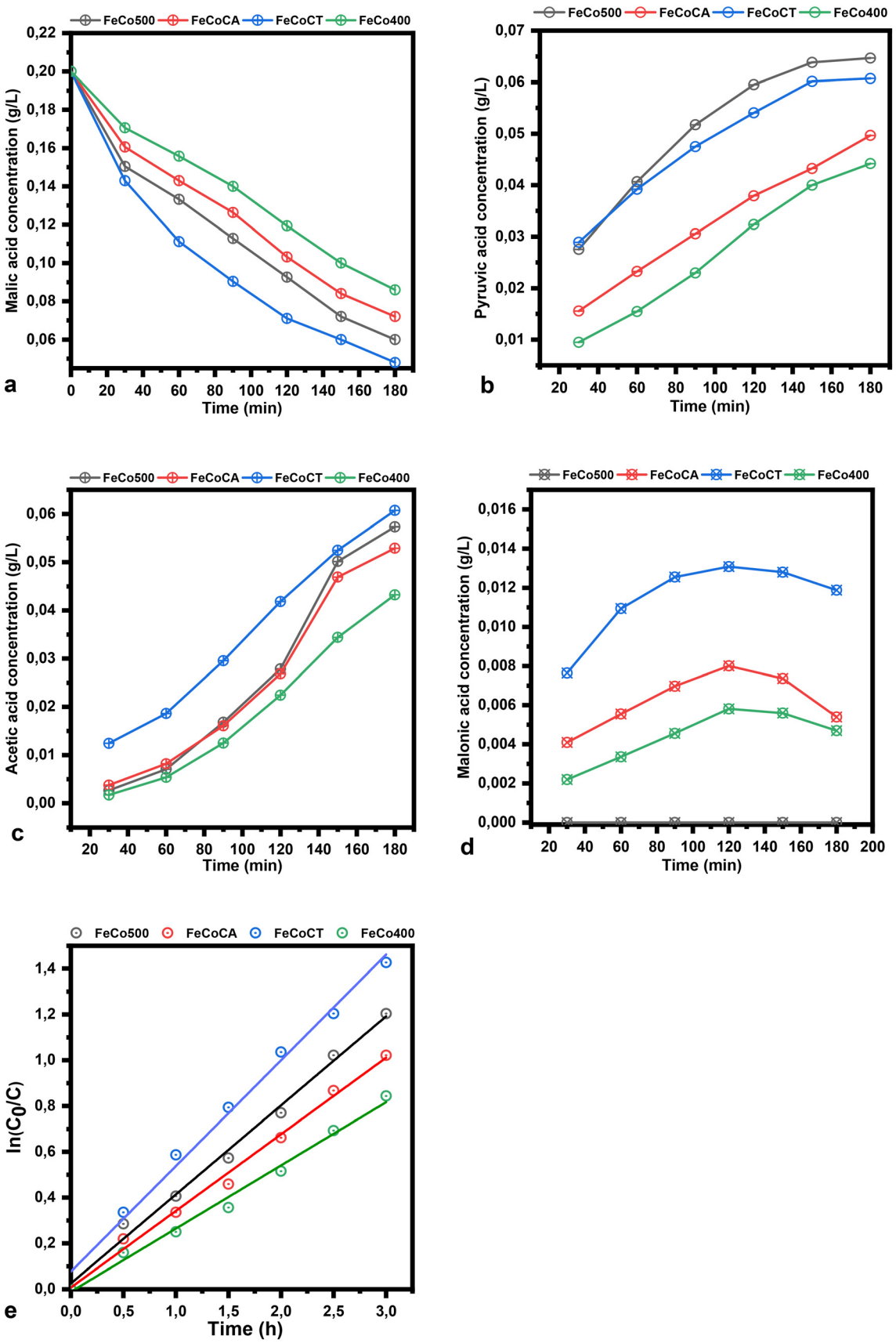

Fig. 9 The plot of malic acid concentration (a), and pyruvic (b), acetic (c) and malonic acid concentration (d) *versus* time (the reaction conditions – solvent: water, temperature: 50 °C, catalyst loading: 1%, air flow: 20 mL min^{-1}, stirring speed: 400 rpm); $ln(C_0/C)$ *versus* time plot (e).

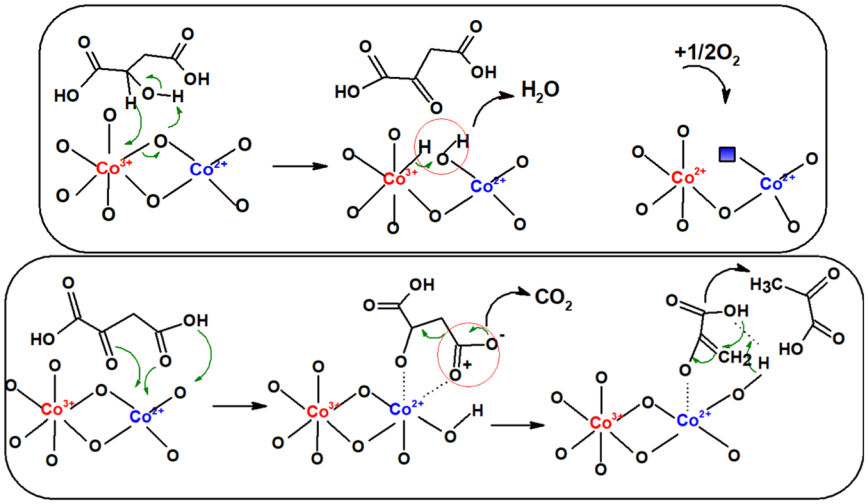

Scheme 3 Mechanism of malic acid conversion over iron-doped Co_3O_4 catalysts.

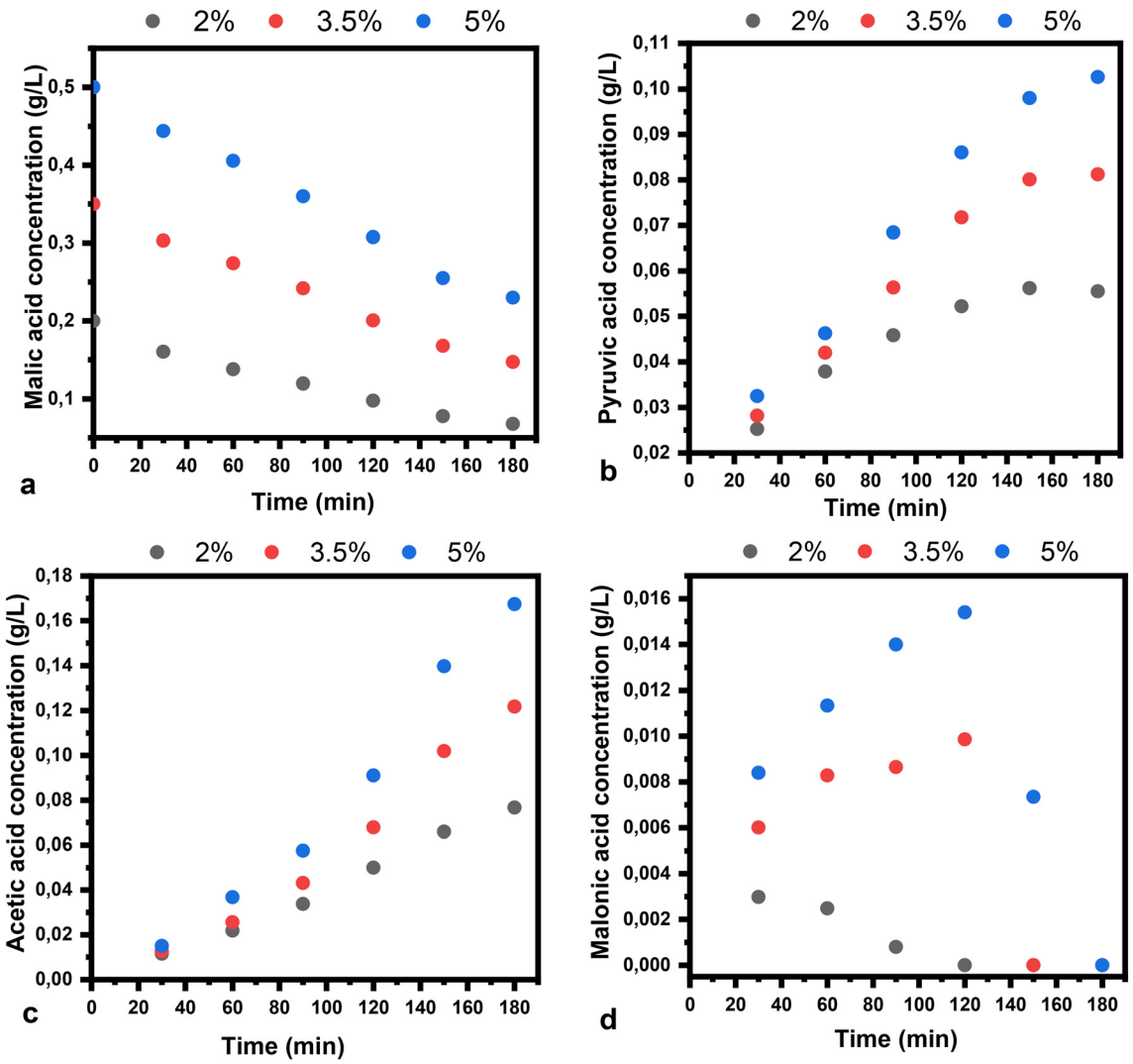

Fig. 10 The plot of malic acid concentration (a), and pyruvic (b), acetic (c) and malonic acid concentration (d) *versus* time over the FeCo500 sample (the reaction conditions – solvent: ethanol, temperature: 50 °C, catalyst loading: 1%, air flow: 20 mL min^{-1}, stirring speed: 400 rpm).

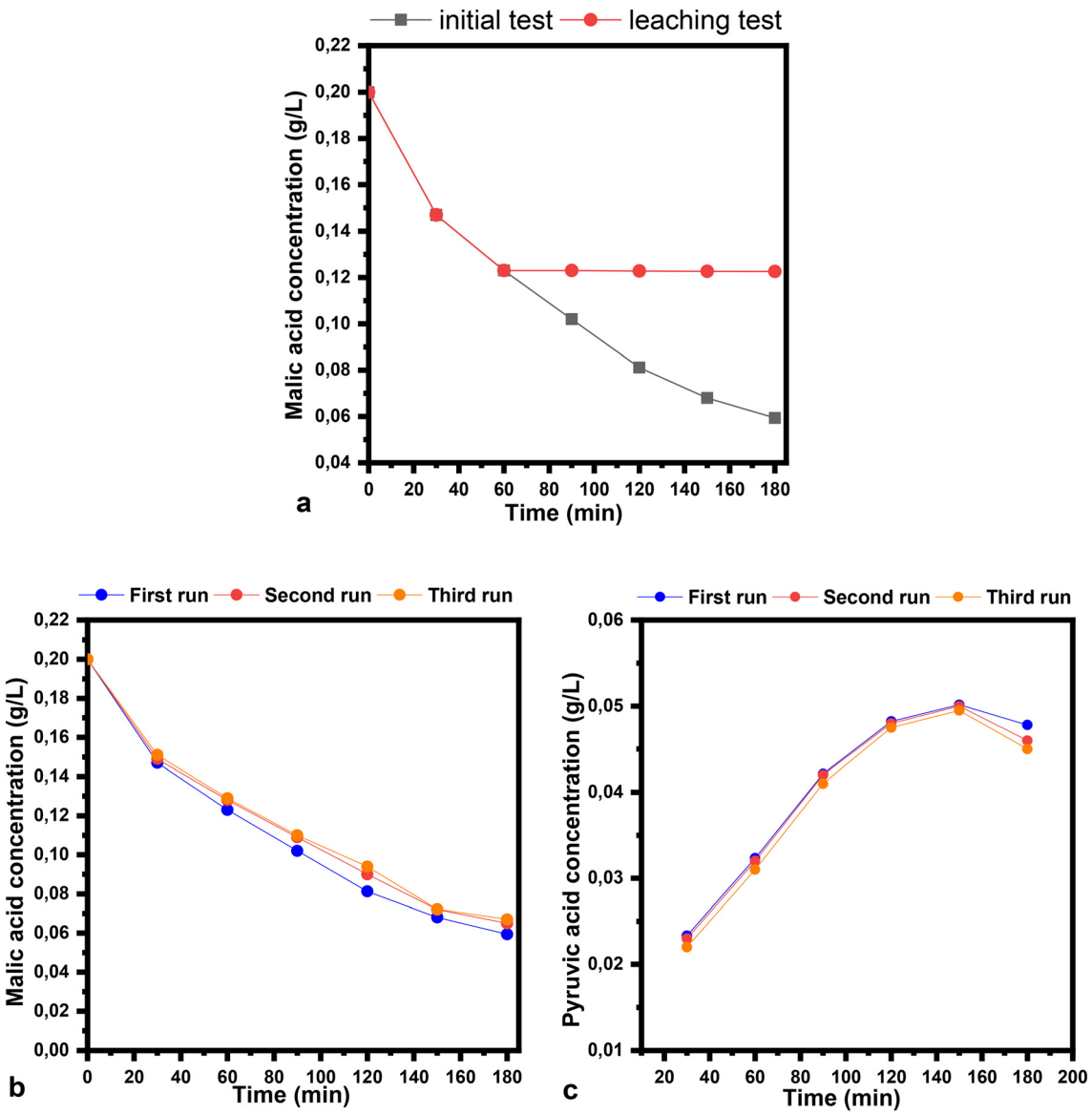

Fig. 11 Stability and recyclability tests of malic acid conversion over the CoFeCT sample: leaching test (a), malic acid concentration (b), and pyruvic acid concentration (c) *versus* time (the reaction conditions; solvent: ethanol, temperature: 50 °C, catalyst loading: 1%, air flow: 20 mL min^{-1}, stirring speed: 400 rpm).

reactions proceeding through the Mars van Krevelen mechanism.

Under the applied conditions, the results follow first-order reaction kinetics, in agreement with the equation:

$$\frac{-dC}{dt} = k \cdot C$$

where C represents malic acid concentration and k is the experimental first-order reaction rate constant. A linear plot of $\ln(C_0/C)$ *versus* time has been observed (Fig. 8e) and k could be determined from the slope, its values being 3.6×10^{-1} h^{-1}, 3.2×10^{-1} h^{-1}, 4.0×10^{-1} h^{-1} and 2.6×10^{-1} h^{-1}, respectively, higher than those obtained by Danion *et al.*[56] for malic acid conversion by photodegradation.

The plots of malic acid and product concentration in water as a solvent are illustrated in Fig. 9. The catalysts used have the same trend in water as in ethanol, but present a higher conversion of malic acid in water. The concentration of pyruvic acid when water is used as a solvent is higher compared to the use of ethanol, while the acetic acid concentration in the same conditions decreased. The rate constant in water has the following values: 3.9×10^{-1} h^{-1}, 3.3×10^{-1} h^{-1}, 4.6×10^{-1} h^{-1} and 2.8×10^{-1} h^{-1}, respectively.

The mechanism of the reactions occurring during the oxidative dehydrogenation/decarboxylation of malic acid is shown in Scheme 3. We suppose that the reaction intermediate is oxaloacetic acid obtained in the oxidative dehydrogenation of alcohol function, through the transfer of electrons between Co^{3+} centers and the hydrogen bound to

the carbon atom to which the hydroxyl group is located, and between the hydrogen of the OH group and the oxygen of the catalyst, with the appearance of an oxygen vacancy quickly filled with oxygen from the reaction medium. Since oxaloacetic acid was not found in our reaction products, we can infer that its transformation into pyruvic acid and later into acetic acid is fast. The transformation of oxaloacetic acid into pyruvic acid is done through a stable cycle of five atoms between Co^{2+} centers and the oxygen atoms of the carbonyl group and of the carboxyl group from the β position, the ketonic complex being the active species in the decarboxylation stage.

Effect of malic acid concentration. The influence of malic acid concentration in ethanol on its conversion and the concentration of the reaction products has been investigated for the FeCo500 sample and the results are illustrated in Fig. 10. As shown, the concentration of malic acid is halved after 90 min when its initial concentration in ethanol solution is 2%, whereas the conversion to 50% takes longer for the other initial concentrations of 3.5% and 5%. The evolutions of the pyruvic acid and acetic acid concentrations exhibit similar trends, irrespective of the malic acid concentration. The concentration of pyruvic acid seems to reach a maximum after 150 minutes, whereas the concentration of acetic acid increases continuously over time, with the highest values obtained for a 5% malic acid in ethanol concentration. After 120 minutes, the malonic acid concentration begins to fall, most likely due to its transformation into acetic acid.

The stability and recyclability tests were performed over the CoFeCT samples in ethanol as a solvent (Fig. 11). The leaching studies were performed under optimized conditions. The removal of the catalyst from the reaction mixture was achieved after one hour, at a malic acid conversion of 38.5%. Inductively coupled plasma analysis of the reaction filtrate revealed that the presence of Co was <4 ppm, with no iron being detected. The reaction filtrate was stirred for a longer time, with almost no further conversion being detected (Fig. 11a). For the recyclability studies, three successive runs were carried out on the CoFeCT sample. The spent catalyst was washed with ethanol and dried at 100 °C for 12 h. The final concentrations of malic and pyruvic acid were very little affected in the second and third cycles compared to the initial study (Fig. 11b and c).

4. Conclusions

The transformation of malic acid into pyruvic acid and then into acetic acid was carried out using iron-doped Co_3O_4 spinel-type oxides that had been prepared using the coprecipitation method. The preparation procedure was carried out both with and without surfactants such as citric acid and cetyltrimethylammonium bromide (CTAB). The CoFeCT and CoFe500 samples, with a normal and inverse spinel structure induced by iron, have the highest level of activity (malic acid conversion 70% and 66%, respectively). This occurs as a direct consequence of the replacement of octahedral positions occupied by Co^{3+} ions with Fe^{2+} ions and of tetrahedral positions occupied by Co^{2+} ions with Fe^{3+} ions. A good correlation was also observed between the activity of the catalysts, the optical band gap energy and the presence of additional Co^{2+} sites on the surface. The conversion of malic acid has been correlated with the electron mobility increasing, whereas the yield of pyruvic acid (27.8%-CoFe500; 20%-CoFeCA; 24%-CoFeCT; 18.8%-CoFe400) has a linear association with oxygen defects, corresponding to the existence of Co^{2+} ions from CoO, which are responsible for their presence.

Conflicts of interest

There are no conflicts to declare.

Acknowledgements

This work was supported by a grant from the Romanian Ministry of Education and Research, CNCS – UEFISCDI, project number PNIII-P4-ID-PCE-2020-0580, within PNCDI III. FN, MF and SN acknowledge the Ministry of Research, Innovation and Digitization, CNCS – UEFISCDI for financial support through project no. PN-III-P4-ID-ERC-2021-0007 and the Core Program 2023–2026 (contract PC3-PN23080303).

References

1 Y. Xu, Y. Zhou, W. Cao and H. Liu, Improved Production of Malic Acid in Aspergillus niger by Abolishing Citric Acid Accumulation and Enhancing Glycolytic Flux, *ACS Synth. Biol.*, 2020, **9**, 1418–1425, DOI: **10.1021/acssynbio.0c00096**.

2 W. Lu, X. Sun, L. Gao, X. Hu, H. Song and B. Kong, Study on the characteristics and mechanism of DL-malic acid in inhibiting spontaneous combustion of lignite and bituminous coal, *Fuel*, 2022, **308**, 122012, DOI: **10.1016/j.fuel.2021.122012**.

3 L. Yao, H. S. Yao, G. X. Xi and Y. Feng, Recycling and synthesis of $LiNi_{1/3}Co_{1/3}Mn_{1/3}O_2$ from waste lithium ion batteries using DL-malic acid, *RSC Adv.*, 2016, **6**(22), 17947–17954, DOI: **10.1039/C5RA25079J**.

4 B. Bharathiraja, I. A. E. Selvakumari, J. Jayamuthunagai, R. P. Kumar, S. Varjani, A. Pandey and E. Gnansounou, Biochemical conversion of biodiesel by-product into malic acid: A way towards sustainability, *Sci. Total Environ.*, 2020, **709**, 136206, DOI: **10.1016/j.scitotenv.2019.136206**.

5 X. L. Chen, Y. C. Wang, X. X. Dong, G. P. Hu and L. M. Liu, Engineering rTCA pathway and C_4-dicarboxylate transporter for L-malic acid production, *Appl. Microbiol. Biotechnol.*, 2017, **101**, 4041–4052, DOI: **10.1007/s00253-017-8141-8**.

6 B. Samira, M. J. Nurhidayatullaili and A. Y. Wageeh, Catalytic conversion of biodiesel derived raw glycerol to value added products, *Renewable Sustainable Energy Rev.*, 2015, **41**, 113–127, DOI: **10.1016/j.rser.2014.08.031**.

7 A. Kövilein, C. Kubisch, L. Cai and K. Ochsenreither, Malic acid production from renewables: a review, *J. Chem. Technol. Biotechnol.*, 2020, **95**, 513–526, DOI: **10.1002/jctb.6269**.

8 A. Danion, J. Disdier, C. Guillard and N. Jaffrezic-Renault, Malic acid photocatalytic degradation using a TiO_2-coated optical fiber reactor, *J. Photochem. Photobiol., A*, 2007, **190**, 135–140, DOI: **10.1016/j.jphotochem.2007.03.022**.

9 W. Irawaty, D. Friedmann, J. Scott and R. Amal, Relationship between mineralization kinetics and mechanistic pathway during malic acid photodegradation, *J. Mol. Catal. A: Chem.*, 2011, **335**, 151–157, DOI: **10.1016/j.molcata.2010.11.027**.

10 P. Xu, J. H. Qiu, C. Gao and C. Q. Ma, Biotechnological routes to pyruvate production, *J. Biosci. Bioeng.*, 2008, **105**, 169–175, DOI: **10.1263/jbb.105.169**.

11 Y. Qin, C. Johnson, L. Liu and J. Chen, Introduction of heterogeneous NADH reoxidation pathways into Torulopsis glabrata significantly increases pyruvate production efficiency, *Korean J. Chem. Eng.*, 2011, **28**, 1078, DOI: **10.1007/s11814-010-0483-1**.

12 R. C. Kerber and M. S. Fernando, α-Oxocarboxylic Acids, *J. Chem. Educ.*, 2010, **87**, 1079–1084, DOI: **10.1021/ed1003096**.

13 S. Gu, Z. Zhao, Y. Yao, J. Li and C. Tian, Designing and Constructing a Novel Artificial Pathway for Malonic Acid Production Biologically, *Front. Bioeng. Biotechnol.*, 2022, **9**, 820507, DOI: **10.3389/fbioe.2021.820507**.

14 B. S. Chen, Y. Y. Zeng, L. Liu, L. Chen, P. Duan, R. Luque, R. Ge and W. Zhang, Advances in catalytic decarboxylation of bioderived fatty acids to diesel-range alkanes, *Renewable Sustainable Energy Rev.*, 2022, **158**, 112178, DOI: **10.1016/j.rser.2022.112178**.

15 T. Li, G. Sun, L. Xiong, B. Zheng, Y. Duan, R. Yu, J. Jiang, Y. Wang and W. Yang, Transition-metal-free decarboxylation of D-glucaric acid to furan catalyzed by $SnCl_4$ in a biphasic system, *Mol. Catal.*, 2021, **516**, 111958, DOI: **10.1016/j.mcat.2021.111958**.

16 K. Avasthi, A. Bohre, M. Grilc, B. Likozar and B. Saha, Advances in catalytic production processes of biomass-derived vinyl monomers, *Catal. Sci. Technol.*, 2020, **10**, 5411–5437, DOI: **10.1039/D0CY00598C**.

17 A. Bohre, U. Novak, M. Grilc and B. Likozar, Synthesis of bio-based methacrylic acid from biomass-derived itaconic acid over barium hexa-aluminate catalyst by selective decarboxylation reaction, *Mol. Catal.*, 2019, **476**, 110520, DOI: **10.1016/j.mcat.2019.110520**.

18 Y. Teng, L. X. Song, L. B. Wang and J. Xia, Face-Raised Octahedral Co_3O_4 Nanocrystals and Their Catalytic Activity in the Selective Oxidation of Alcohols, *J. Phys. Chem. C*, 2014, **118**, 4767–4773, DOI: **10.1021/jp412175t**.

19 R. Zhong, Q. Wang, L. Du, Y. Pu, S. Ye, M. Gu, Z. C. Zhang and L. Huang, Ultrathin polycrystalline Co_3O_4 nanosheets with enriched oxygen vacancies for efficient electrochemical oxygen evolution and 5-hydroxymethylfurfural oxidation, *Appl. Surf. Sci.*, 2022, **584**, 152553, DOI: **10.1016/j.apsusc.2022.152553**.

20 C. Chen, Z. Zhou, J. Liu, B. Zhu, H. Hu, Y. Yang, G. Chen, M. Gao and J. Zhang, Sustainable biomass upgrading coupled with H_2 generation over in-situ oxidized Co_3O_4 electrocatalysts, *Appl. Catal., B*, 2022, **307**, 121209, DOI: **10.1016/j.apcatb.2022.121209**.

21 P. Jia, T. Yang, Q. Liu, J. Yan, T. Shen, L. Zhang, Y. Liu, X. Zhao, Z. Gao, J. Wang, Y. Tang and J. Huang, In-situ imaging Co_3O_4 catalyzed oxygen reduction and evolution reactions in a solid state Na-O_2 battery, *Nano Energy*, 2020, **77**, 105289, DOI: **10.1016/j.nanoen.2020.105289**.

22 D. W. Wang, Q. H. Wang and T. M. Wang, Morphology controllable synthesis of cobalt oxalates and their conversion to mesoporous Co_3O_4 nanostructures for application in supercapacitors, *Inorg. Chem.*, 2011, **50**, 6482–6492, DOI: **10.1021/ic200309t**.

23 X. W. Lou, D. Deng, J. Y. Lee, J. Feng and L. A. Archer, Self supported formation of needle like Co_3O_4 nanotubes and their application as lithium-ion battery electrodes, *Adv. Mater.*, 2008, **20**, 258–262, DOI: **10.1002/adma.200702412**.

24 A. L. Bhatti, A. Tahira, A. Gradone, R. Mazzaro, V. Morandi, U. Aftab, M. I. Abroc, A. Nafady, K. Qi, A. Infantes-Molina, A. Vomiero and Z. H. Ibupoto, Nanostructured Co_3O_4 electrocatalyst for OER: The role of organic polyelectrolytes as soft templates, *Electrochim. Acta*, 2021, **398**, 139338, DOI: **10.1016/j.electacta.2021.139338**.

25 M. Salavati-Niasari and A. Khansari, Synthesis and characterization of Co_3O_4 nanoparticles by a simple method, *C. R. Chim.*, 2014, **17**, 352–358, DOI: **10.1016/j.crci.2013.01.023**.

26 A. Rumplecker, F. Kleitz, E. L. Salabas and F. Schüth, Hard templating pathways for the synthesis of nanostructured porous Co_3O_4, *Chem. Mater.*, 2007, **19**, 485–496, DOI: **10.1021/cm0610635**.

27 Y. Wang, J. C. Shi, J. L. Cao, G. Sun and Z. Y. Zhang, Synthesis of Co_3O_4 nanoparticles via the CTAB-assisted method, *Mater. Lett.*, 2011, **65**, 222–224, DOI: **10.1016/j.matlet.2010.09.090**.

28 J. Deng, L. Kang, G. Bai, Y. Li, P. Li, X. Liu, Y. Yang, F. Gao and W. Liang, Solution combustion synthesis of cobalt oxides(Co_3O_4 and Co_3O_4/CoO) nanoparticles as supercapacitor electrode materials, *Electrochim. Acta*, 2014, **132**, 127–135, DOI: **10.1016/j.electacta.2014.03.158**.

29 A. Singhal, A. Bisht, A. Kumar and S. Sharma, One pot, rapid synthesis of Co_3O_4 by solution combustion method and its electrochemical properties in different electrolytes, *J. Electroanal. Chem.*, 2016, **776**, 152–161, DOI: **10.1016/j.jelechem.2016.07.004**.

30 K. Kim, H. Kim, Y. Park, G. Ahn, C. Kim and J. Park, Evolution of structural and magnetic properties and the electronic structure of spinel $Fe_xCo_{3x}O_4$ thin films, *IEEE Trans. Magn.*, 2005, **41**(10), 3478–3480, DOI: **10.1109/TMAG.2005.854914**.

31 V. O'Shea, R. Nafria, P. Ramírez and N. Homs, Development of robust Co-based catalysts for the selective H_2-production by ethanol steam-reforming. The Fe-promoter effect, *Int. J.*

Hydrogen Energy, 2008, **33**, 3601–3606, DOI: **10.1016/j.ijhydene.2007.10.049**.

32 Q. Yang, P. Cui, Q. Ye, S. Chen and Z. Wu, X-ray absorption study of the geometry structure of Co^{2+}/Co^{3+} in ammonia solution, *J. Mol. Struct.*, 2015, **1098**, 306–310, DOI: **10.1016/j.molstruc.2015.06.034**.

33 A. Gallo-Cordova, J. Ovejero, A. Pablo-Sainz-Ezquerra, J. Cuya, B. Jeyadevan, S. Veintemillas-Verdaguer, P. Tartaj and M. del Puerto Morales, Unravelling an amine-regulated crystallization crossover to prove single/multicore effects on the biomedical and environmental catalytic activity of magnetic iron oxide colloids, *J. Colloid Interface Sci.*, 2022, **608**, 1585–1597, DOI: **10.1016/j.jcis.2021.10.111**.

34 M. A. Garcia, F. Jiménez-Villacorta, A. Quesada, J. de la Venta, N. Carmona, I. Lorite, J. Llopis and J. F. Fernández, Surface magnetism in ZnO/Co_3O_4 mixtures, *J. Appl. Phys.*, 2010, **107**, 043906, DOI: **10.1063/1.3294649**.

35 A. Djemai, G. Calas and J. P. Muller, Role of structural Fe(III) and iron oxide nanophases in mullite coloration, *J. Am. Ceram. Soc.*, 2001, **84**(7), 1627–1631, DOI: **10.1111/j.1151-2916.2001.tb00887.x**.

36 A. B. Getsoian, Z. Zhai and A. T. Bell, Band-Gap Energy as a Descriptor of Catalytic Activity for Propene Oxidation over Mixed Metal Oxide Catalysts, *J. Am. Chem. Soc.*, 2014, **136**, 13684–13697, DOI: **10.1021/ja5051555**.

37 X. Wang, X. Chen, L. Gao, H. Zheng, Z. Zhang and Y. Qian, One-Dimensional Arrays of Co_3O_4 Nanoparticles: Synthesis, Characterization, and Optical and Electrochemical Properties, *J. Phys. Chem. B*, 2004, **108**, 16401–16404, DOI: **10.1021/jp048016p**.

38 L. Qiao, H. Y. Xiao, H. M. Meyer, J. N. Sun, C. M. Rouleau, A. A. Puretzky, D. B. Geohegan, I. N. Ivanov, M. Yoon, W. J. Weber and M. D. Biegalski, Nature of the band gap and origin of the electro−/photo-activity of Co_3O_4, *J. Mater. Chem. C*, 2013, **1**, 4628, DOI: **10.1039/C3TC30861H**.

39 R. M. Obodo, A. Nwanya, A. B. C. Ekwealor, I. Ahmad, T. Zhao, R. U. Osuji, M. Maaza and F. I. Ezema, Influence of pH and annealing on the optical and electrochemical properties of cobalt(III) oxide(Co_3O_4) thin films, *Surf. Interfaces*, 2019, **16**, 114–119, DOI: **10.1016/j.surfin.2019.05.006**.

40 C. M. Jiang, L. R. Baker, J. M. Lucas, J. Vura-Weis, A. P. Alivisatos and S. Leone, Characterization of Photo-Induced Charge Transfer and Hot Carrier Relaxation Pathways in Spinel Cobalt Oxide(Co_3O_4), *J. Phys. Chem. C*, 2014, **118**, 22774–22784, DOI: **10.1021/jp5071133**.

41 L. Wang, E. Guan, Y. Wang, L. Wang, Z. Gong, Y. Cui, X. Meng, B. C. Gates and F. S. Xiao, Silica accelerates the selective hydrogenation of CO_2 to methanol on cobalt catalysts, *Nat. Commun.*, 2020, **11**, 1033, DOI: **10.1038/s41467-020-14817-9**.

42 U. Caudillo-Flores, I. Barba-Nieto, M. Muñoz-Batista, A. Kubacka and M. Fernández-García, Characterization of photo-catalysts: from traditional to advanced approaches, *Top. Curr. Chem.*, 2019, **377**, 24, DOI: **10.1007/s41061-019-0248-1**.

43 A. Pradeep, P. Priyadarshini and G. Chandrasekaran, Structural, magnetic and electrical properties of nanocrystalline zinc ferrite, *J. Alloys Compd.*, 2011, **509**, 3917–3923, DOI: **10.1016/j.jallcom.2010.12.168**.

44 I. Luisetto, F. Pepe and E. Bemporad, Preparation and characterization of nano cobalt oxide, *J. Nanopart. Res.*, 2008, **10**, 59–67, DOI: **10.1007/s11051-008-9365-4**.

45 S. J. Kashyap, R. Sankannavar and G. M. Madhu, Iron oxide(Fe_2O_3) synthesized via solution-combustion technique with varying fuel-to-oxidizer ratio: FT-IR, XRD, optical and dielectric characterization, *Mater. Chem. Phys.*, 2022, **286**, 126118, DOI: **10.1016/j.matchemphys.2022.126118**.

46 M. Ziemba, C. Schilling, M. V. Ganduglia-Pirovano and C. Hess, Toward an Atomic-Level Understanding of Ceria-Based Catalysts: When Experiment and Theory Go Hand in Hand, *Acc. Chem. Res.*, 2021, **54**, 2884–2893, DOI: **10.1021/acs.accounts.1c00226**.

47 S. M. Ansari, K. C. Ghosh, R. S. Devan, D. Sen, P. U. Sastry, Y. D. Kolekar and C. V. Ramana, Eco-Friendly Synthesis, Crystal Chemistry, and Magnetic Properties of Manganese-Substituted $CoFe_2O_4$ Nanoparticles, *ACS Omega*, 2020, **5**, 19315–19330, DOI: **10.1021/acsomega.9b02492**.

48 S. M. Ansari, B. B. Sinha, K. R. Pai, S. K. Bhat, Y. R. Ma, D. Sen, Y. D. Kolekar and C. V. Ramana, Controlled surface/interface structure and spin enabled superior properties and biocompatibility of cobalt ferrite nanoparticles, *Appl. Surf. Sci.*, 2018, **459**, 788–801, DOI: **10.1016/j.apsusc.2018.08.063**.

49 K. B. Modi, P. Y. Raval, S. J. Shah, C. R. Kathad, S. V. Dulera, M. V. Popat, K. B. Zankat, K. G. Saija, T. K. Pathak, N. H. Vasoya, V. K. Lakhani, U. Chandra and P. K. Jha, Raman and Mossbauer Spectroscopy and X-ray Diffractometry Studies on Quenched Copper–Ferri–Aluminates, *Inorg. Chem.*, 2015, **1**, 2851–2859, DOI: **10.1021/ic502497a**.

50 G. Mitran, A. Urda, O.-D. Pavel, S. Neatu, M. Florea and F. Neatu, A green way for pyruvic acid synthesis from biomass-derived L-malic acid on tetrahedral versus octahedral cobalt sites/hematite, *Biomass Convers. Biorefin.*, 2022, DOI: **10.1007/s13399-022-02513-1**.

51 N. A. Rashid, C. Haw, W. Chiu, N. H. Khanis, A. Rohaizad, P. S. Khiew and S. A. Rahman, Structural-and optical-properties analysis of single crystalline hematite(α-Fe_2O_3) nanocubes prepared by one-pot hydrothermal approach, *CrystEngComm*, 2016, **18**, 4720–4732, DOI: **10.1039/C6CE00573J**.

52 R. K. Bera, H. Parka and R. Ryoo, Co_3O_4 nanosheet on zeolite-templated carbon as an efficient oxygen electrocatalyst for zinc-air battery, *J. Mater. Chem. A*, 2019, **7**, 9988–9996, DOI: **10.1039/C9TA01482A**.

53 P. M. Kouotou, A. El Kasmi, L. N. Wu, M. Waqas and Z. Y. Tian, Particle size-band gap energy-catalytic properties relationship of PSE-CVD-derived Fe_3O_4 thin films, *J. Taiwan Inst. Chem. Eng.*, 2018, **93**, 427–435, DOI: **10.1016/j.jtice.2018.08.014**.

54 A. El Kasmi, Z. Y. Tian, H. Vieker, A. Beyer and T. Chafik, Innovative CVD synthesis of Cu_2O catalysts for CO oxidation, *Appl. Catal., B*, 2016, **186**, 10–18, DOI: **10.1016/j.apcatb.2015.12.034**.

55 B. Y. Jibril, Catalytic performances and correlations with metal oxide band gaps of metal-tungsten mixed oxide catalysts in propane oxydehydrogenation, *React. Kinet. Catal. Lett.*, 2005, **86**, 171–177, DOI: **10.1007/s11144-005-0309-z**.

56 A. Danion, J. Disdier, C. Guillard and N. Jaffrezic-Renault, Malic acid photocatalytic degradation using a TiO_2-coated optical fiber reactor, *J. Photochem. Photobiol., A*, 2007, **190**, 135–140, DOI: **10.1016/j.jphotochem.2007.03.022**.

